CHEMISTRY
AN ASIAN JOURNAL

Supporting Information

A Low-Temperature Molecular Precursor Approach to Copper-Based Nano-Sized *Digenite* Mineral for Efficient Electrocatalytic Oxygen Evolution Reaction

Biswarup Chakraborty[+], Shweta Kalra[+], Rodrigo Beltrán-Suito, Chittaranjan Das, Tim Hellmann, Prashanth W. Menezes,* and Matthias Driess*This manuscript is part of a special collection in honor of the 2nd International Conference on Organometallics and Catalysis (ICOC-2020). .

Electronic Supplementary Information (ESI) for:

A Low-Temperature Molecular Precursor Approach to Copper-Based Nano-Sized *Digenite* Mineral for the Efficient Electrocatalytic Oxygen Evolution Reaction

Table of Contents

Characterization

Single-Crystal X-ray Structure Determination: Single crystal of **[{(PyHS)$_2$Cu^I(pySH)}$_2$](OTf)$_2$ (1) (CCDC no. 1975340)** was mounted on a glass capillary in perfluorinated oil and measured in a cold N_2 flow. The data of all compounds were collected on an Oxford Diffraction SuperNova, Single source at the offset, Atlas at 150 K (Cu-Kα radiation, λ = 1.54184 Å). The structures were solved by direct methods and refined on F2 with the SHELX-97[1] and X-Seed[2] software packages. The positions of all the H atoms were calculated and refined isotropically according to a riding model. In the molecular structure of **1**, one triflate ($CF_3SO_3^-$) anion is positioned in a special symmetry position and the overall anion is disordered over two positions with an approximate half (0.5) occupancy of all the atoms. Compound **1** is a di-nuclear complex where the whole cationic unit is symmetry generated by its half asymmetric unit and symmetry-related atoms have been labeled as ′ symbol (-x+3/2, -y+1/2, -z+1/2). Mercury 3.9 software package was used for molecular view and drawing.

Powder X-ray diffraction (PXRD). Cu_9S_5 was characterized by PXRD on an STOE Stadi-P with Cu-$K_{\alpha 1}$ source (λ = 1.54058 Å), curved Ge(111)-monochromator and DECTRIS MYTHEN 1K detector.

Inductively coupled plasma atomic emission spectroscopy (ICP-AES). ICP-AES was conducted on a Thermo Jarrell Ash Trace Scan analyzer. The materials were digested in aqua regia HCl: HNO_3 4:1 v/v (nitric acid, SUPRA-Qualität ROTIPURAN® Supra 69% and hydrochloric acid, SUPRA-Qualität ROTIPURAN® Supra 30%) and the average of three reproducible independent experiments is reported. The digestion volume (2.5 mL) was diluted with Milli-Q water up to 15 mL. Calibration curves were prepared for copper and selenium with concentrations between 1 mg L^{-1} and 100 mg L^{-1} from standard solutions (1000 mg L^{-1} Single-Element ICP-Standard Solution ROTI STAR).

Scanning electron microscopy (SEM). SEM images were collected on a GeminiSEM500 NanoVP microscope (ZEISS) integrated with an EDX detector (Bruker Quantax XFlash® 6|60). The most abundant elements were selected from the EDX spectrum. Data handling and analysis were achieved with the software package EDAX. The SEM experiments were conducted at the Zentrum für Elektronenmikroskopie (ZELMI) of the TU Berlin.

Transmission electron microscopy (TEM). TEM was performed on an FEI Tecnai G2 20 S-TWIN transmission electron microscope (FEI Company, Eindhoven, Netherlands) equipped with a LaB_6 source at 200 kV acceleration voltage. For the investigation of the films after electrocatalysis, the films were scraped from the electrode substrate and transferred onto a carbon-coated copper grid. EDX analyses were achieved with an EDAX r-TEM SUTW detector (Si (Li) detector), and the images were recorded with a GATAN MS794 P CCD camera. The TEM experiments were conducted at the Zentrum für Elektronenmikroskopie (ZELMI) of the TU Berlin.

X-ray photoelectron spectroscopy (XPS). The elemental analysis was done by X-ray photoelectron spectroscopy (XPS). The XPS measurements were done using ThermoFischer's Escalab 250 spectrometer. The samples were excited with monochromatic Al-kα excitation (1486.6 eV), and the photo emitted electrons were collected at the concentric hemispherical analyzer with a pass energy of 10 eV

spectrometer. A magnetic collector lens was used to collect the maximum of photo emitted electrons to the analyzer. The analysis was done using Avantage software from Thermo Fischer.

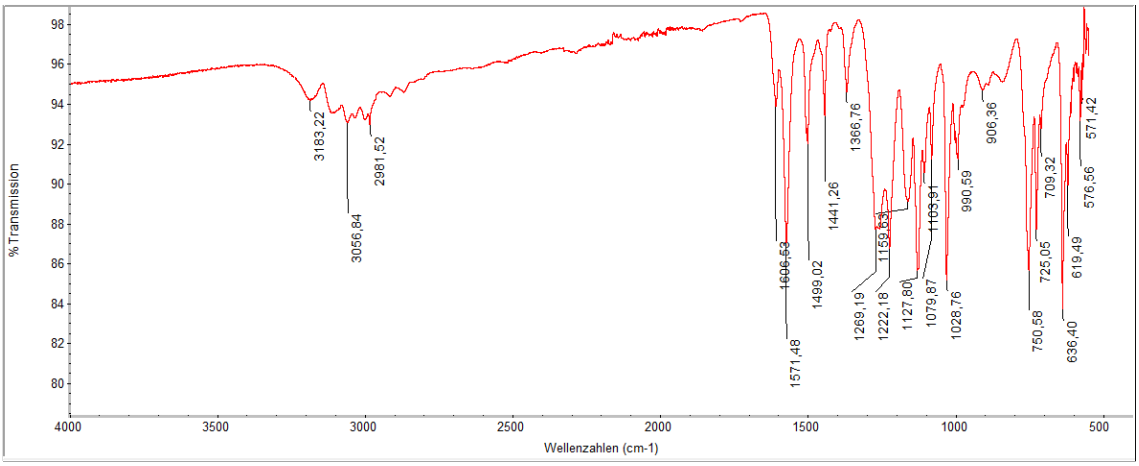

Figure S1. Fourier transformed infrared (FT-IR) spectrum of the as-synthesized **1** (ATR, diamond). Strong vibration at 1127 and 1366 cm^{-1} could be attributed to the vibrations of ν(S=O) and ν(C–F) of triflate ion.[3]

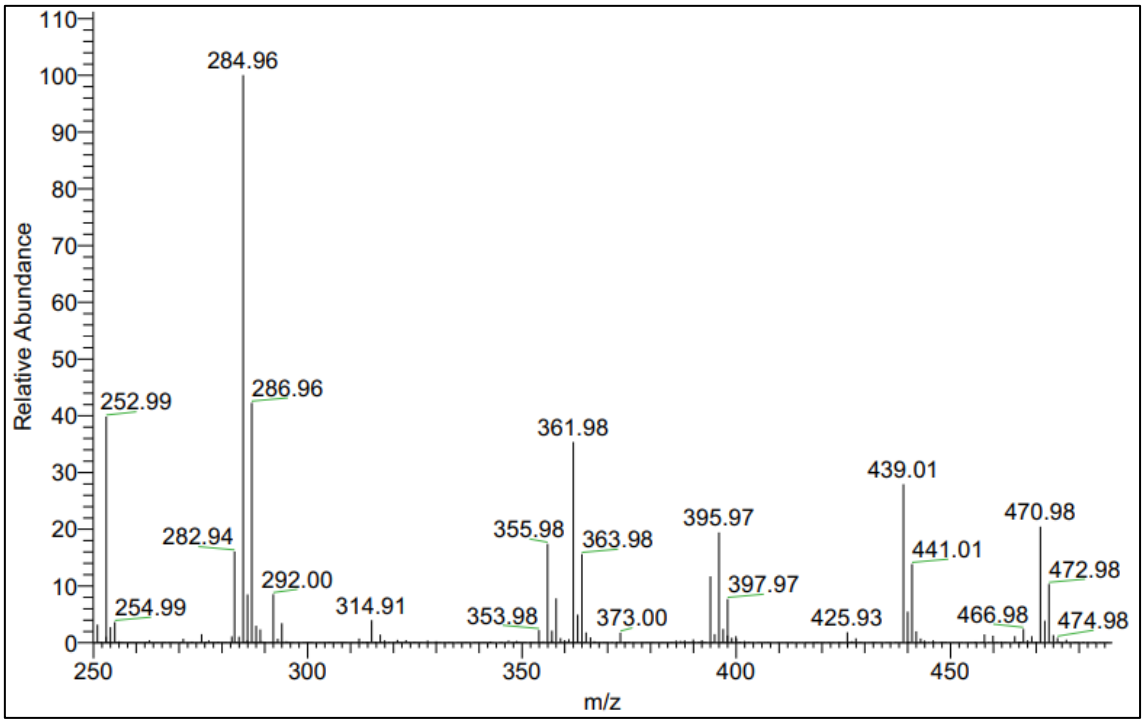

Figure S2. Electron spray ionization-mass spectrum of solution **1** (positive ion mode, in tetrahydrofuran). Major molecular ion peaks at m/z value of 284.96, 361.98 and 395.97 with an expected isotopic distribution calculated for the molecular fragments, $[\{(PyHS)_2Cu]^+$, $[\{(PyHS)(PyS)Cu(Py)]^+$ and $[(PyHS)_3Cu]^+$, respectively.

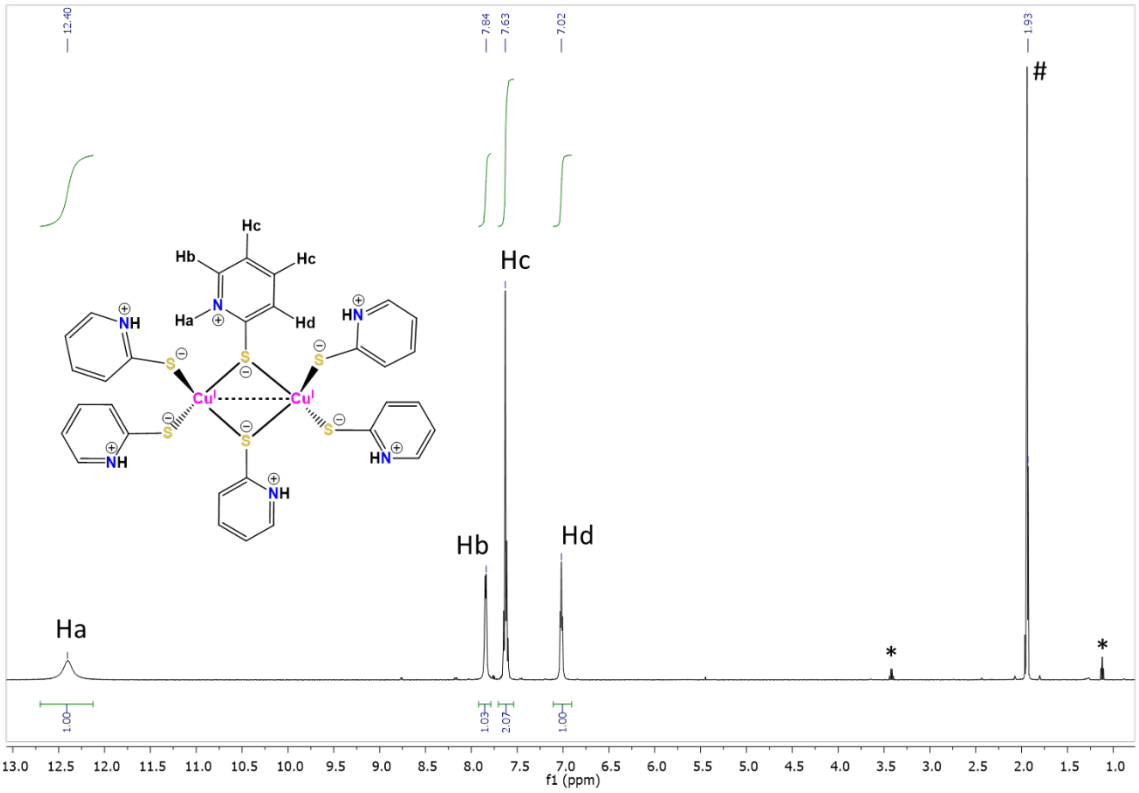

Figure S3. 1-H NMR (in CD_3CN, 500 MHz) spectrum of **1**. The spectrum displays four sets of proton signals from 7.0 ppm to 12.5 ppm assigned to the three aromatic protons (with 1:2:1 relative intensities) and one –NH (pyridinium) proton. (* and # represent the residual Et_2O and CH_3CN in the NMR solvent)

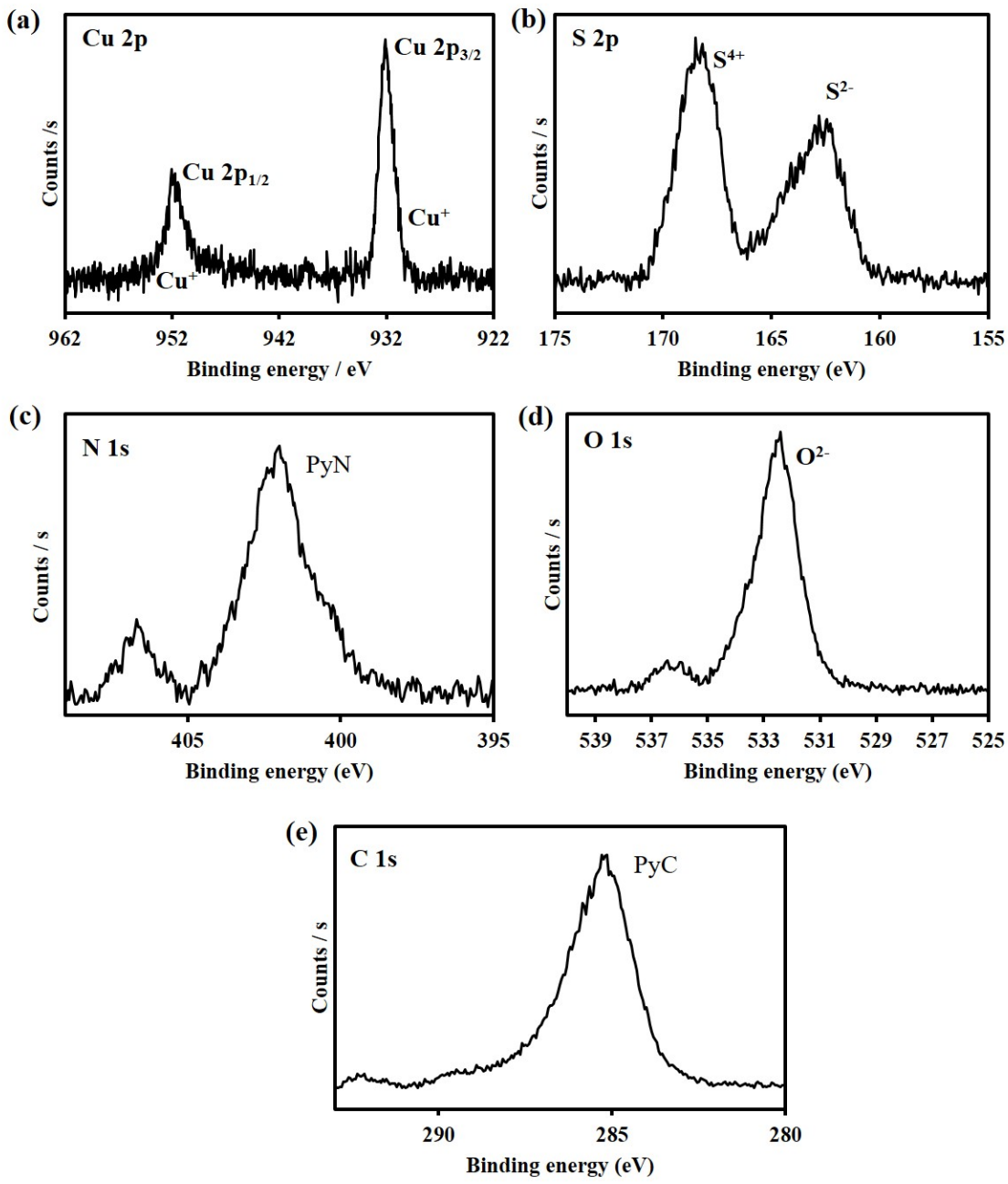

Figure S4. XPS analysis of the as-prepared crystalline powder **1**, (a) core-level Cu 2p, (b) S 2p, (c) N 1s, (d) O 1s, and (e) C 1s spectra. The binding energy values of Cu $2p_{3/2}$ and Cu $2p_{1/2}$ indicated the presence of Cu^{+} in **1**, while the presence of two binding energies for S 2p consistent with S^{4+} of triflate anions.[4] and S^{2-}.[5] of PyHS. The binding energy values of C 1s and N 1s are consistent with the literature aromatic Cand N of pyridine rings.[6]

Table S1. Crystal data and structure refinement for $[\{(PyHS)_2Cu^{I}(PyHS)\}_2](OTf)_2$ (**1**).

Empirical formula	$C_{32}H_{30}Cu_2F_6N_6O_6S_8$
Formula weight	1092.18
Temperature	150.0(1) K
Wavelength	1.54184 Å
Crystal system	Monoclinic
Space group	*I*2/*m*
Unit cell dimensions	*a* = 7.5456(2) Å α= 90°
	b = 28.2525(7) Å β= 94.378(3)°
	c = 19.8600(6) Å γ = 90°
Volume	4221.4(2) Å^3
Z	4
Density (calculated)	1.718 Mg/m^3
Absorption coefficient	5.633 mm^{-1}
F(000)	2208
Crystal size	0.28 x 0.18 x 0.08 mm^3
Theta range for data collection	2.725 to 71.948°
Index ranges	-9<=h<=9, -34<=k<=30, -24<=l<=22
Reflections collected	7828
Independent reflections	4162 [R(int) = 0.0408]
Completeness to theta	71.948° (98.2 %)
Absorption correction	Semi-empirical from equivalents
Max. and min. transmission	1.00000 and 0.04781
Refinement method	Full-matrix least-squares on F^2
Data / restraints / parameters	4162 / 6 / 282
Goodness-of-fit on F^2	1.103
Final R indices [I>2sigma(I)]	R1 = 0.0691, wR2 = 0.1987
R indices (all data)	R1 = 0.0781, wR2 = 0.2096
Largest diff. peak and hole	2.256 and -1.339 e.Å^{-3}

Table S2. Selected bond lengths (Å) and angles (°) around the metal center of the cationic part of **1**.

Bond Lengths	(Å)	Bond Angles	(°)
Cu(1)-S(1)	2.2936(11)	S(1)-Cu(1)-S(2)	123.42(5)
Cu(1)-S(2)	2.3075(12)	S(1)-Cu(1)-S(3)	104.36(4)
Cu(1)-S(3)	2.3152(12)	S(2)-Cu(1)-S(3)	114.72(4)
Cu(1)-S(3)′	2.4964(12)	S(1)-Cu(1)-S(3)′	108.08(4)
Cu(1)-Cu(1)′	2.8567(13)	S(2)-Cu(1)-S(3)′	97.79(4)
S(3)-C(11)	1.727(4)	S(3)-Cu(1)-S(3)′	107.27(4)
S(1)-C(1)	1.714(4)	S(1)-Cu(1)-Cu(1)′	118.18(4)
S(2)-C(6)	1.708(4)	S(2)-Cu(1)-Cu(1)′	117.22(4)
		S(3)-Cu(1)-Cu(1)′	56.56(3)
		S(3)′-Cu(1)-Cu(1)′	50.71(3)

Symmetry transformations used to generate equivalent atoms: (′) -x+3/2,-y+1/2,-z+1/2

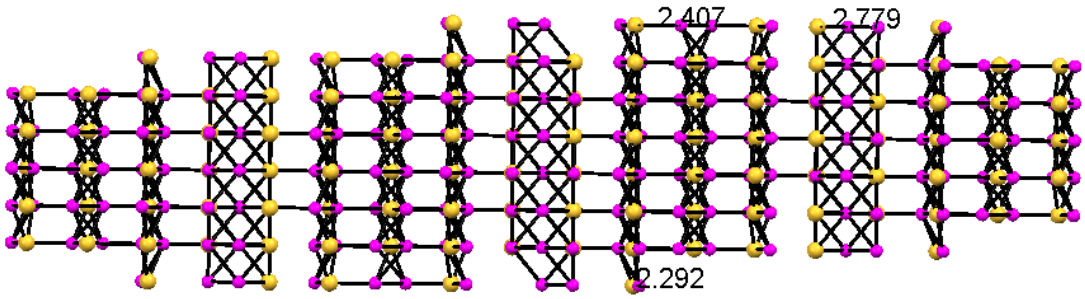

Figure S5. Crystal structure of Digenite Cu_9S_5 (JCPDS-47-1748, rhombohedral, *R*-3*m*). Figure (a) represents the stacked-layer of Cu and S (color code; Cu: purple and S: yellow) with selected bond distances.[5a,7] The values are different Cu-S distances in Å.

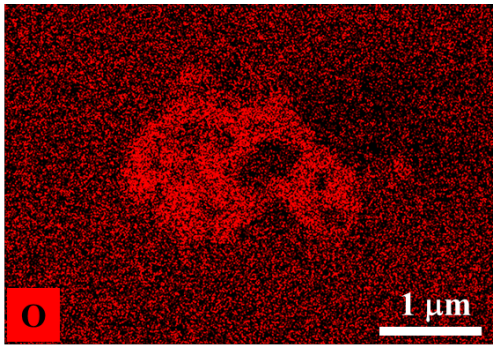

Figure S6. EDX-oxygen mapping of the as-prepared Cu_9S_5 material. (Fe and S mapping in Figure 2e and f). Oxygen apperared from the surface oxidation of the Cu_9S_5 in air.

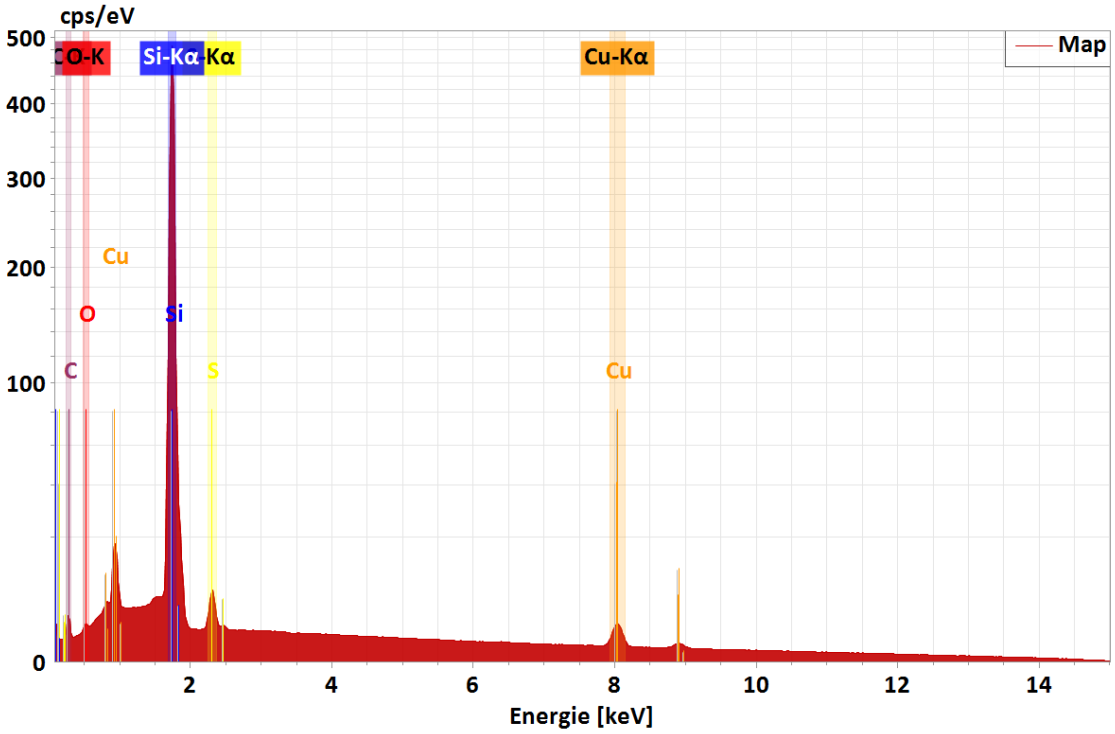

Figure S7. EDX spectrum of Cu_9S_5 confirming the presence of Cu and S (the source of Si peaks was from the Si wafer support used during SEM measurement). Quantitative analysis of elements confirmed an atomic ratio of Cu and S is ~1.8:1.

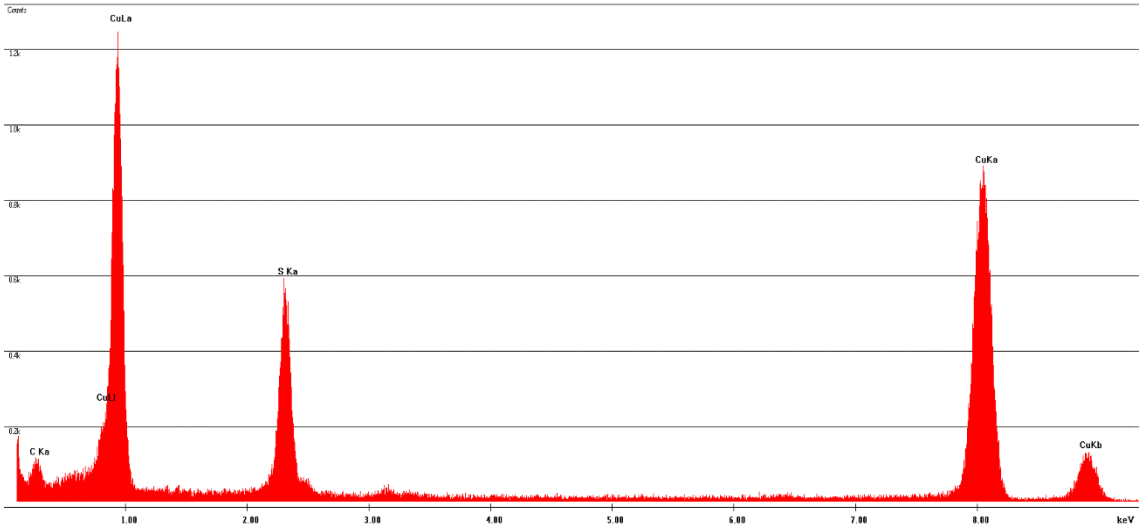

Figure S8. EDX analysis of Cu_9S_5 during TEM measurement. The presence of Cu and S in the spectrum was very similar to that observed during SEM.

Table S3. Quantification of the Cu and S content in the as-prepared Cu_9S_5 by ICP-AES. An average data of three independent measurements are provided herein. The atomic ratio of copper and sulfide obtained from ICP-AES matches perfectly (1.83:1) with that obtained from SEM-EDX.

Material	**Cu:S (ICP-AES)**	**Cu:S (SEM-EDX)**
Cu_9S_5	1.83:1.00	1.8:1

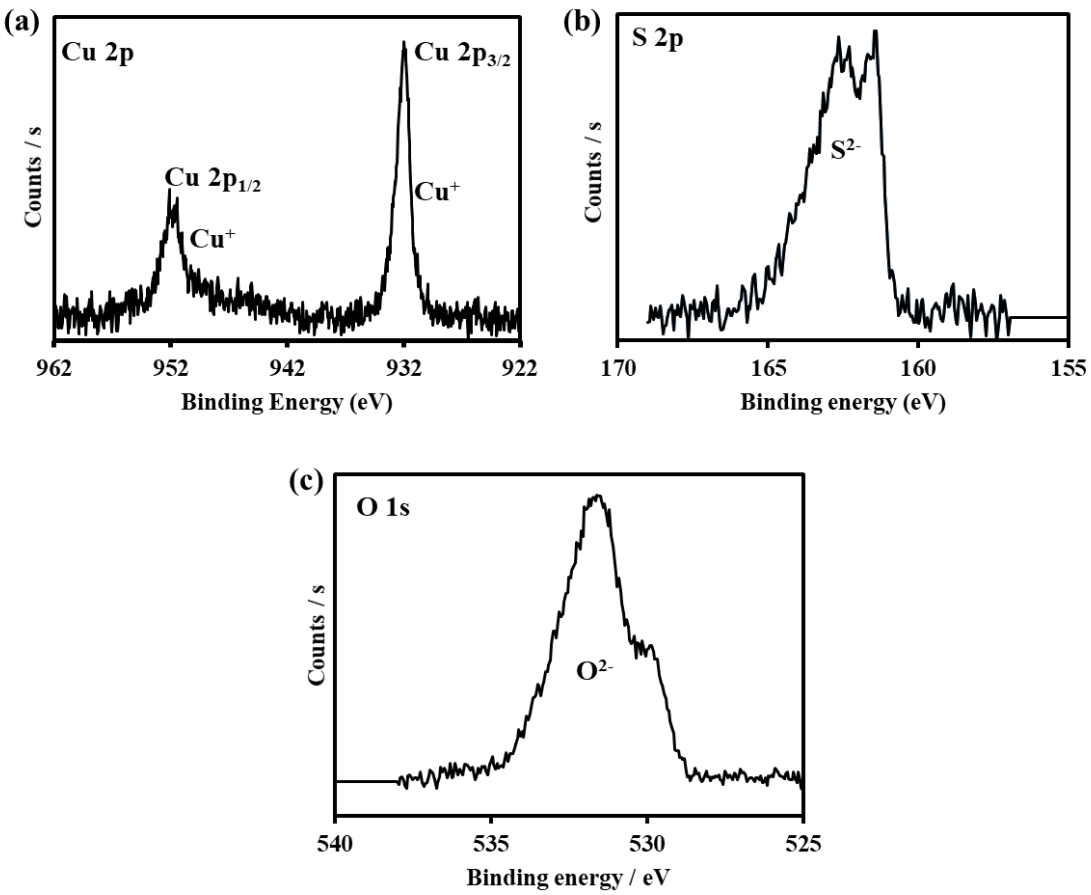

Figure S9. XPS spectra of as-synthesized Cu_9S_5; (a) Cu 2p, (b) S 2p and (c) O 1s. Both Cu $2p_{3/2}$ and Cu $2p_{1/2}$ revealed two major peaks and the peaks centered at a binding energy of 931.85 and 951.6 eV could be assigned to Cu^+ that are characteristic of a Cu_9S_5 and Cu_xS material.[5] The broad S 2p spectrum exhibited a binding energy of 161.95 eV, which confirmed the presence of S^{2-}.[5] The peak for O 1s indicate the oxidation of Cu_9S_5 due to slow oxidation in air.[5]

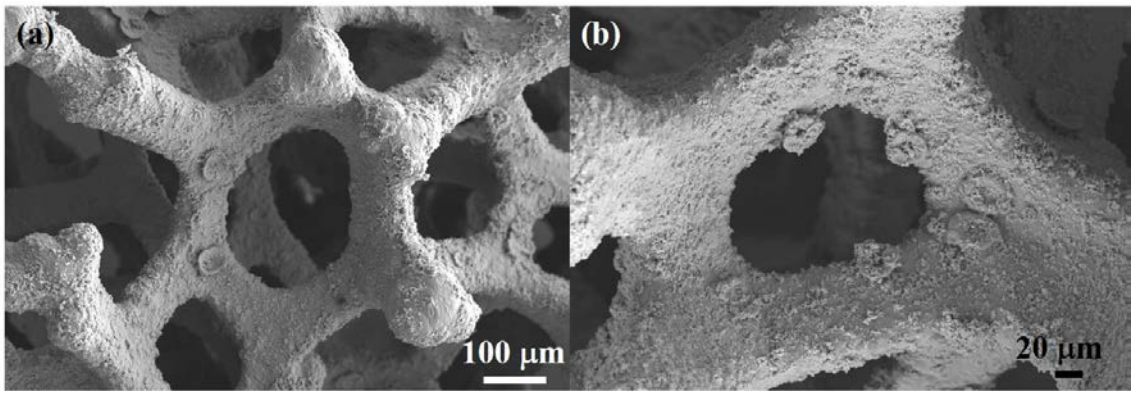

Figure S10. SEM images of the Cu_9S_5 deposited on nickel foam (NF), which revealed a homogeneous distribution of the particles over the three-dimensional NF substrate.

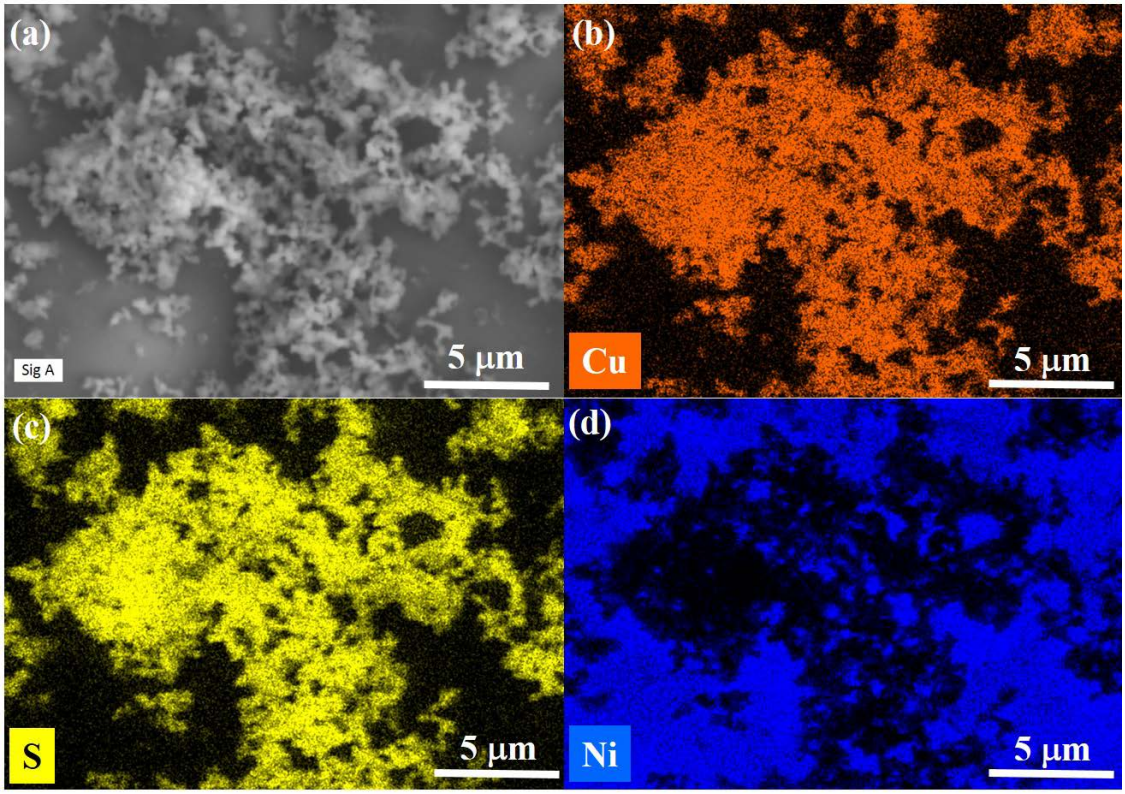

Figure S11. Elemental mapping of Cu_9S_5 deposited on NF; (a) SEM image of the selected region of NF and elemental mapping (b) Cu (orange), (c) S (yellow), and (d) Ni (blue). The SEM image and elemental mapping confirmed the homogenous distribution of Cu and S on the deposited CuS particles on NF confirmed the chemical stability of the material under electrophoretic deposition (EPD) conditions.

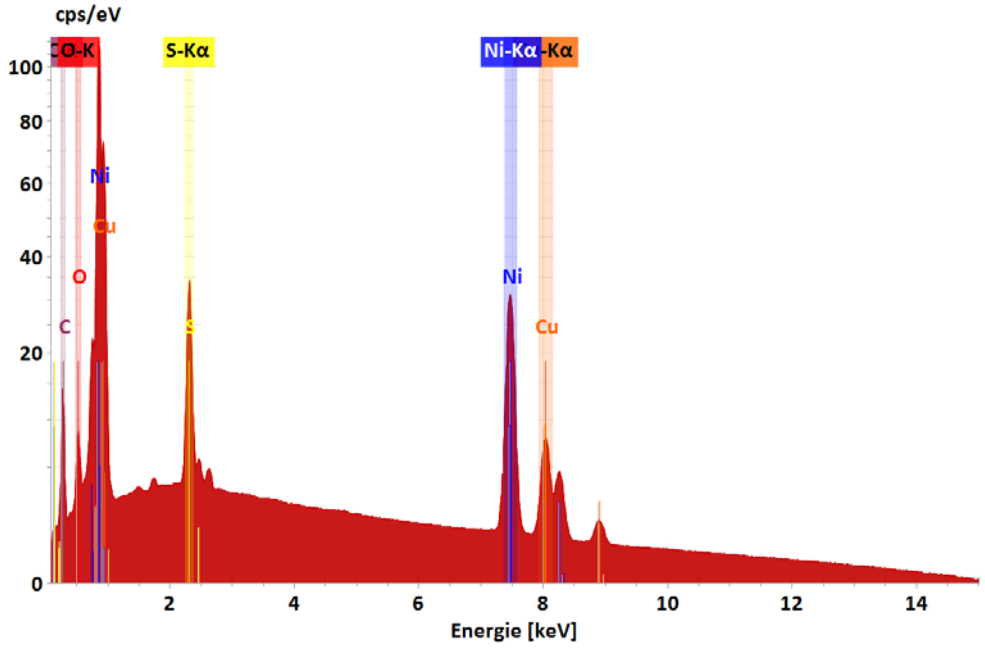

Figure S12. EDX analysis of the deposited Cu_9S_5 on NF confirmed the presence of Cu and S in an appropriate ratio (1.80:1). A large contribution of Ni peaks is from the NF.

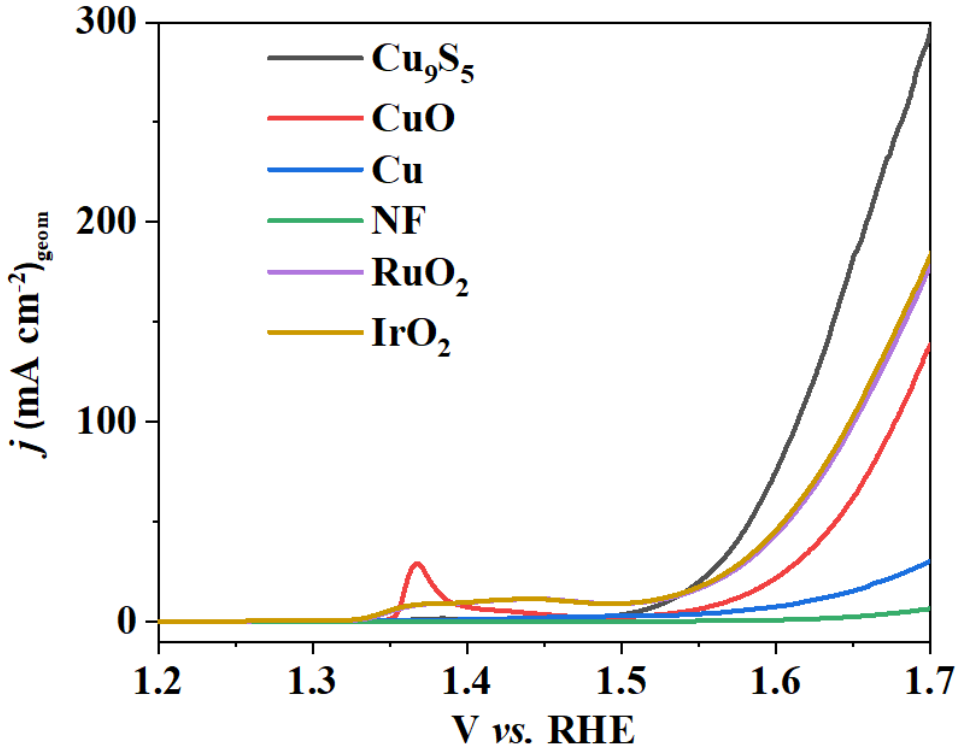

Figure S13. Polarization curves obtained from LSV measurement during OER studied with Cu_9S_5/NF in comparison to copper-based materials, Cu and CuO, and other benchmark catalysts RuO_2 and IrO_2. LSV measurements were recorded under identical experimental conditions (scan rate: 1 mV s^{-1}, electrolyte 1M KOH, materials deposited on NF).

Table S4. Electrocatalytic OER (in 1 M KOH) of Cu_9S_5 in compare to different Cu-based catalysts and benchmark $NiFeO_x$ catalysts.

Catalyst	Substrate	j (mA cm^{-2})	η (mV) [a]	References
Cu_9S	NF	10	298	This work
CuO	NF	10	339	This work
Cu	NF	10	389	This work
Cu_9S	FTO	10	380	This work
CuO	FTO	10	440	This work
Cu	FTO	10	>550	This work
CuO	CF	10	338	[8]
Cu_2S	CF	20	336	[5b]
Cu_2S	C [b]	10	410	[9]
CuO	FTO	10	475	[10]
CuO	FTO	1	530	[11]
CuO	GC [c]	10	420	[12]
CuO–TCNQ	CF [d]	25	317	[13]
Cu_3P NB	Cu [e]	10	380	[14]
Cu_3P	NF	10	320	[15]
$Ni_{59}Cu_{19}P_9$	Cu	10	307	[16]
Co-CuO	CF [d]	50	299	[17]
$NiFe_2O_4$	GC	10	290	[18]
$NiFeO_x$	GC	10	328	[19]
$Fe_xNi_{1-x}O$	Au/QCM[f]	10	297	[20]
Fe-doped NiO_x	GC	10	310	[21]
NiO_x-Fe	NF	10	215	[22]
RGO/Ni-FeOOH	FTO	10	260	[23]
CoFe hydroxide	NF	10	220	[24]
NiO	Au/QCM[f]	1	305	[25]
CoO_x	GC	10	315	[26]

[a] overpotential. [b] carbon fiber, [c] glassy carbon, [d] copper foam, [e] copper foam, [f] quartz crystal microbalance (QCM)

Table S5. Resistance to charge transfer R_{CT} (Ω) of Cu_9S_5/NF, compared to CuO/NF, and Cu/NF. The R_{CT} values were obtained from the fitting of the semicircle in the Nyquist plots (Figure 2c on the main text).

Material	R_{CT} (Ω)
Cu_9S_5/NF	9.5
CuO/NF	13.4
Cu/NF	15.0

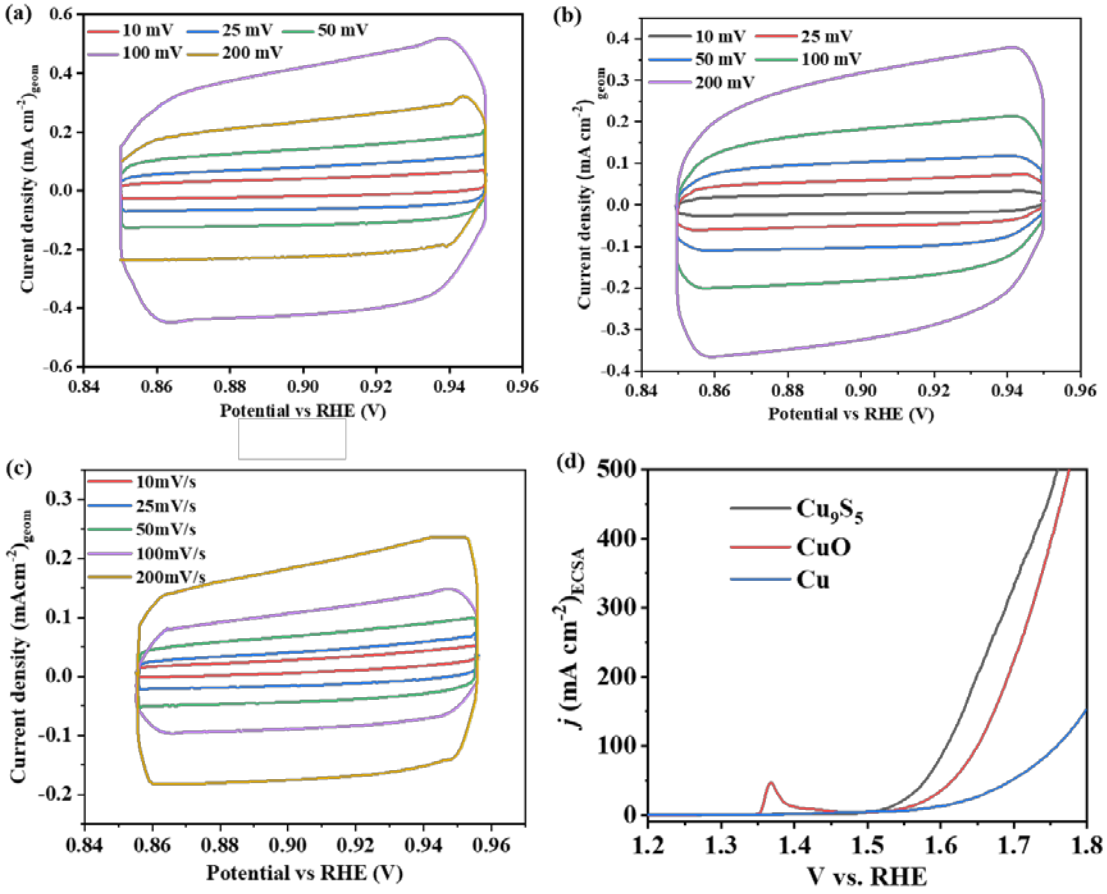

Figure S14. The double-layer capacitance (C_{dl}) determination for the prepared materials. CV scans in a non-Faradaic potential range of as-prepared (a) Cu_9S_5/NF, (b) CuO/NF, (c) Cu/NF electrodes in 1 M KOH at a scan rate of 10 mV s^{-1}, 25 mV s^{-1}, 50 mV s^{-1}, 100 mV s^{-1} and 200 mV s^{-1}. Half of the differences in current density variation ($\Delta J = (J_{anodic}-J_{cathodic})/2$) at a potential of 0.90 V vs. RHE plotted against scan rate fitted to a linear regression that allows the determination of double-layer capacitance (C_{dl}) (Figrue 3d, main text).[27] The ECSA was then calculated by using the C_{dl} and the specific capacitance of the material (C_s) per unit area (1.7 mF cm^{-2}). The values of ECSA (tabulated in Table S5) provide information on the catalytic active sites favoring the efficient adsorption and transfer of reactants to enhance the electrochemical reaction.[28] (d) ECSA normalized current density versus potential plot reveals a better intrinsic activity of he Cu_9S_5 over copper based catalysts used herein.

Table S6. Double-layer capacitance (C_{dl}) and ECSA values determined (electrochemically) for Cu_9S_5, Cu and CuO (deposited on NF). The correlation factor (R^2) of the linear plot of the capacitive current vs. scan rate is 0.99 to 1.00.[27b]

Material	R^2	C_{dl} (mF cm^{-2})	ECSA (cm^2)
Cu_9S_5/NF	1.00	1.51	0.89
CuO/NF	0.99	1.05	0.62
Cu/NF	0.99	0.98	0.58

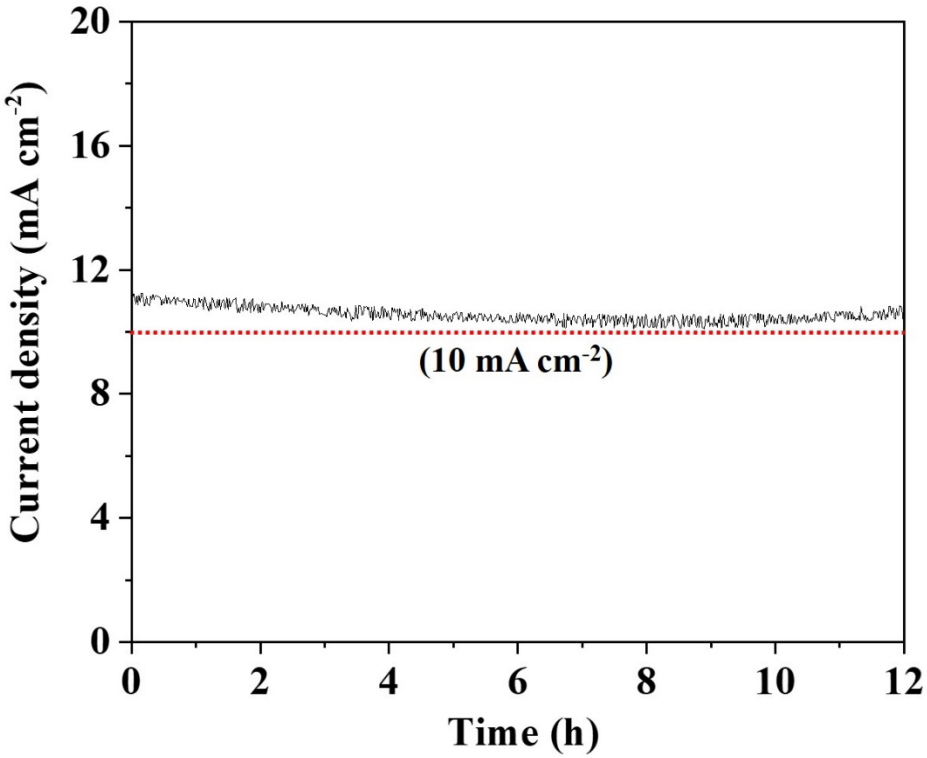

Figure S15. OER CA profile of Cu_9S_5/NF in aqueous 1 M KOH solution at an applied potential of 1.55 V (vs. RHE). A small drop in current density of of Cu_9S_5 can be ascribed to the slow transformation of the catalyst (loss of S in to the electorlyte) by finally forming an active CuO@Cu_9S_5 catalyst with high stability.

Calculation of Faradaic efficiency. The Faradaic efficiency (FE) towards OER in 1 M KOH was measured in a two-electrode configuration where Cu_9S_5/NF was used as anode and Pt as cathode in a closed electrochemical cell. The electrolyte and cell were first degassed with argon (Ar) for 30 min under constant stirring. Afterward, a constant current density of 50 mA cm^{-2} was applied for a specified period. At the end of electrolysis, the gaseous samples were drawn from the headspace by a gas-tight syringe and analyzed by a GC calibrated for O_2. Each injection was repeated at least three times, and the average value is presented.

The FE is calculated based on:

$$FE(O_2, \%) = \frac{V_{O_2} \times 4 \times F}{V_m \times j \times t} \times 100\%$$

V_{O_2} are the evolved volume of oxygen, F is the Faraday constant (96485.33289 C/mol), V_m is the molar volume of the gas, j is the current density (50 mA cm^{-2}) and t is the time period of electrolysis (360 s).

Table S7. Calculation of Faradaic efficiency for Cu_9S_5/NF.

	j (mA cm^{-2})	**t (s)**	**V_{O_2} (mL)**	**FE (O_2, %)**
Cu_9S_5/NF	50	360	1.06	96

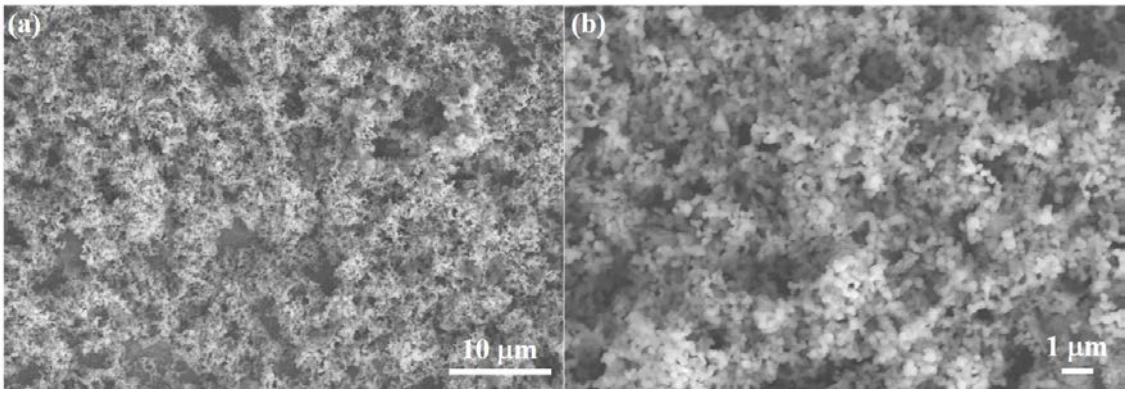

Figure S16. SEM images (in two different magnifications) of Cu_9S_5 deposited on the FTO surface, which represent a homogeneous distribution on the electrode surface.

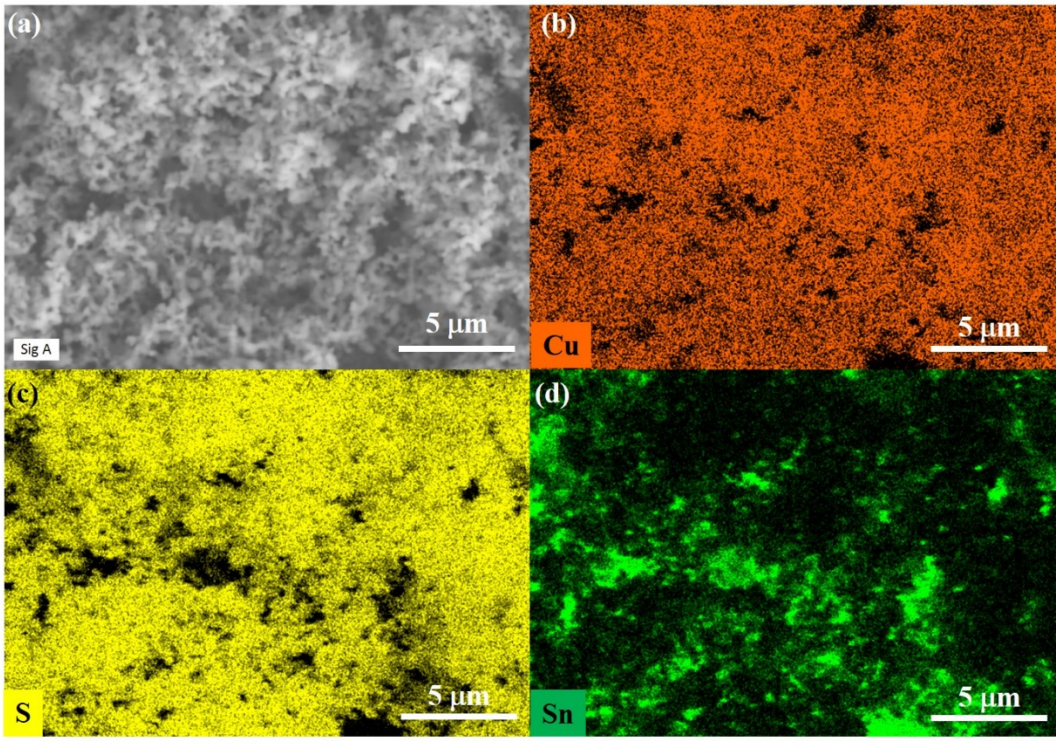

Figure S17. (a) SEM and elemental mapping of (b) Cu (orange), (c) S (yellow) and (d) Sn (green) of as-deposited Cu_9S_5/FTO. The homogenous distribution of Cu and S was observed in the material particles. The Sn appeared from FTO as the background from the electrode.

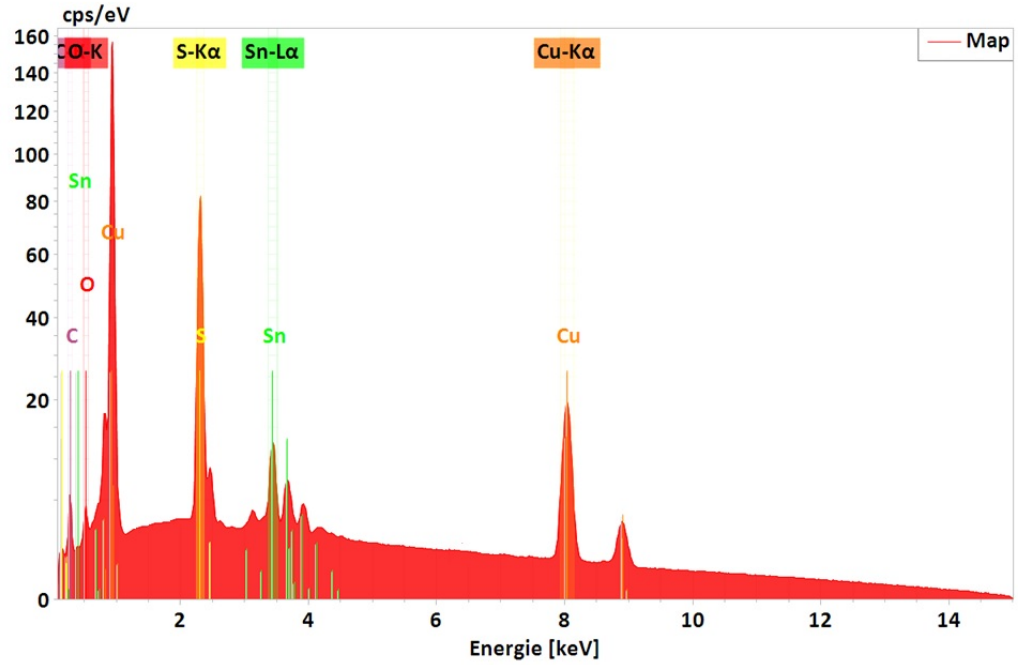

Figure S18. EDX spectrum of the Cu_9S_5 film on FTO that confirms the presence of Cu and S with an atomic ratio of ca. 1.79:1. The elemental composition confirms the structural integrity of the material after EPD. The Sn peaks appeared from FTO (as the background of the material).

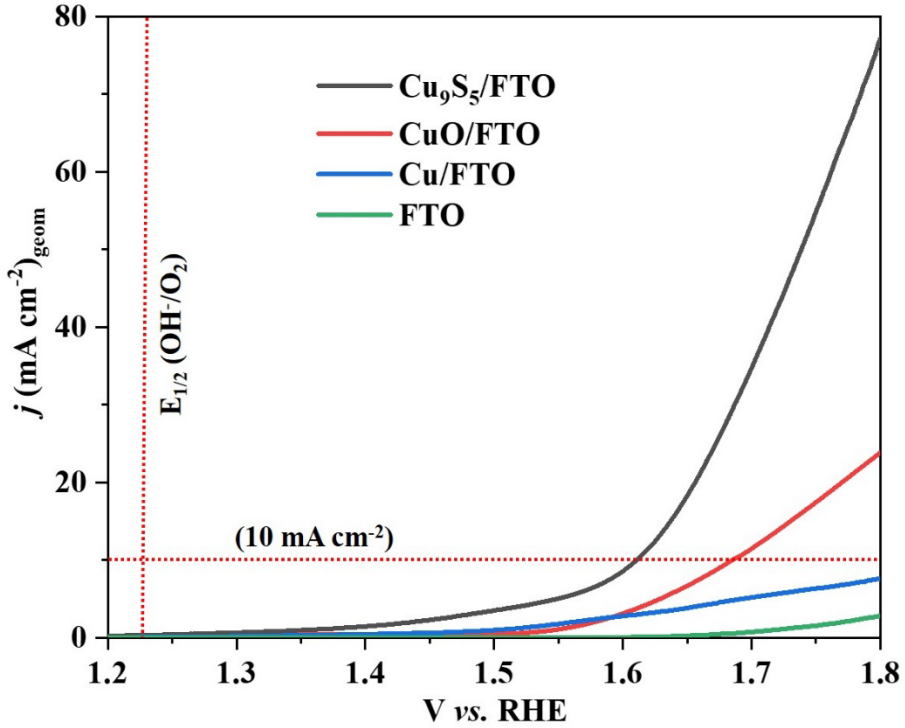

Figure S19. OER polarization curve of OER with Cu_9S_5, Cu, and CuO deposited on the FTO surface. The lowest overpotential (380 mV) was recorded at 10 mA cm^{-2} for Cu_9S_5, and the trend of OER (with respect to overpotentials) is very similar to that observed on NF.

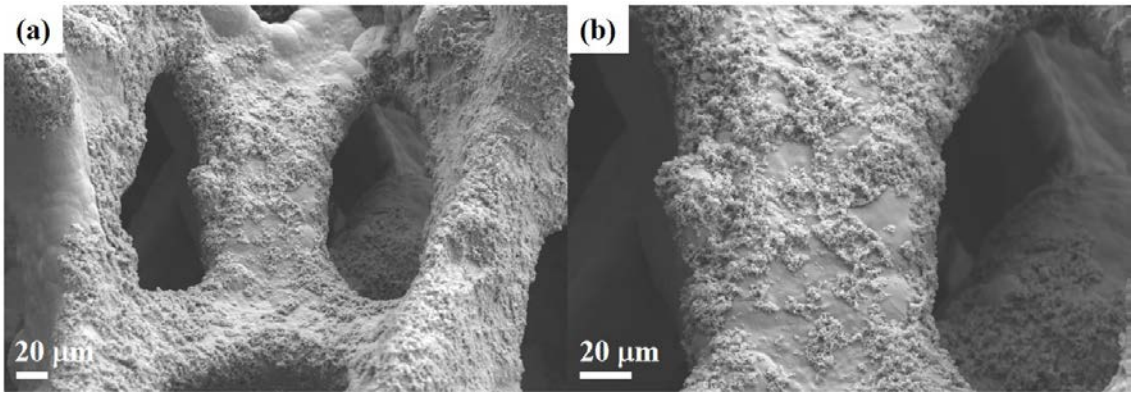

Figure S20. SEM images after OER CA of the Cu_9S_5 deposited on which depicts no abrupt change in the structural integrity of Cu_9S_5 on the three-dimensional NF.

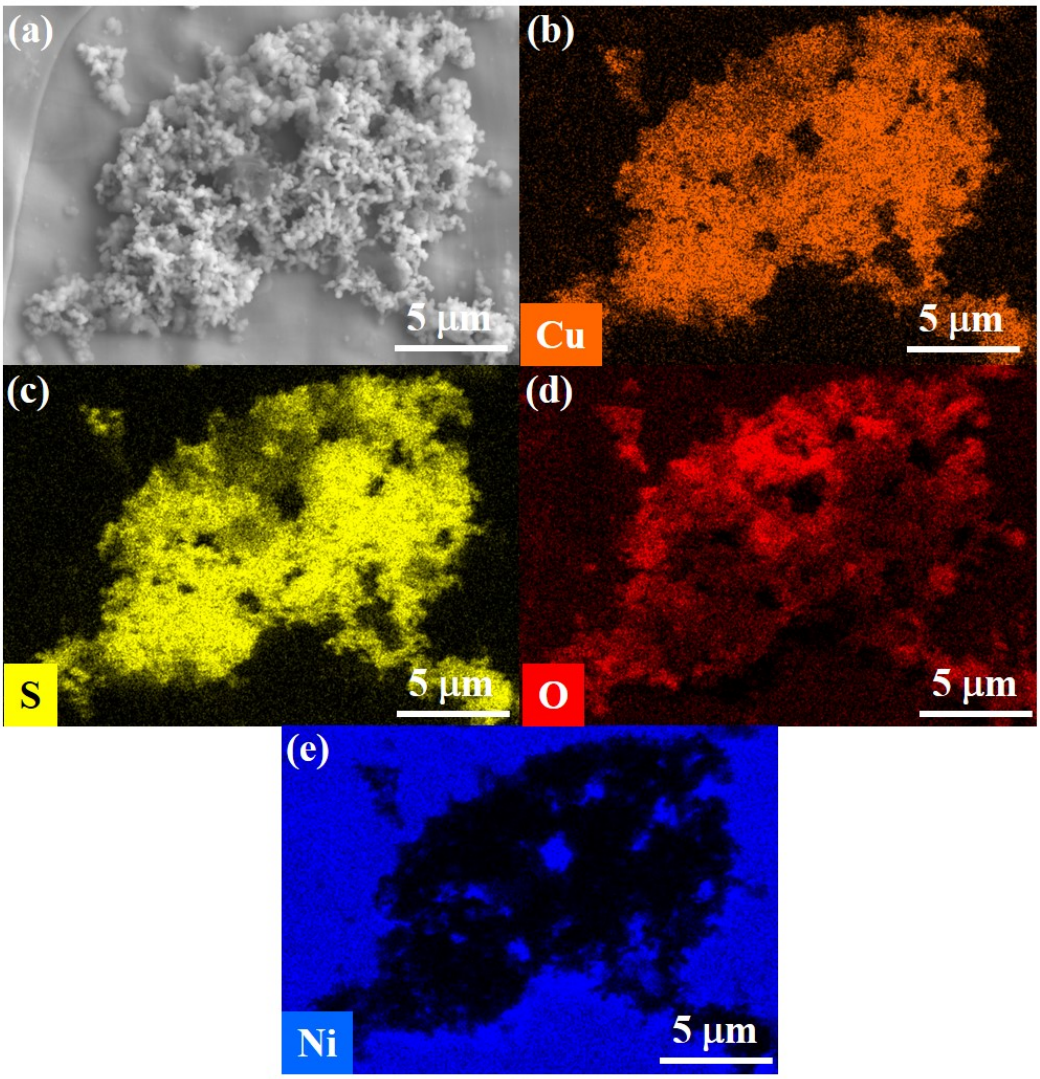

Figure S21. (a) SEM and elemental mapping of Cu_9S_5 (b) Cu (orange), (c) S (yellow), (d) O (red), and (e) Ni (blue) after OER CA. The elements Cu and S were homogenously distributed, indicating that both elements are present after catalysis. Substantial incorporation of O into the structure was found.

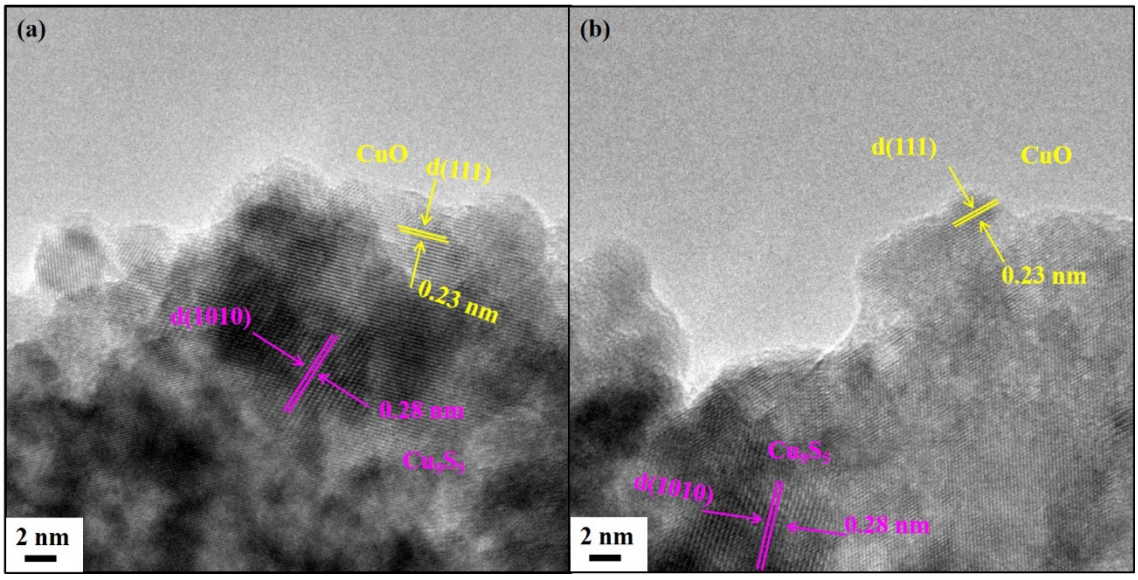

Figure S22. High-resolution TEM image after OER showing the crystalline phase of Cu_9S_5 along with crystalline overlayer CuO (JCPDS 72-629) near the edges.[11]

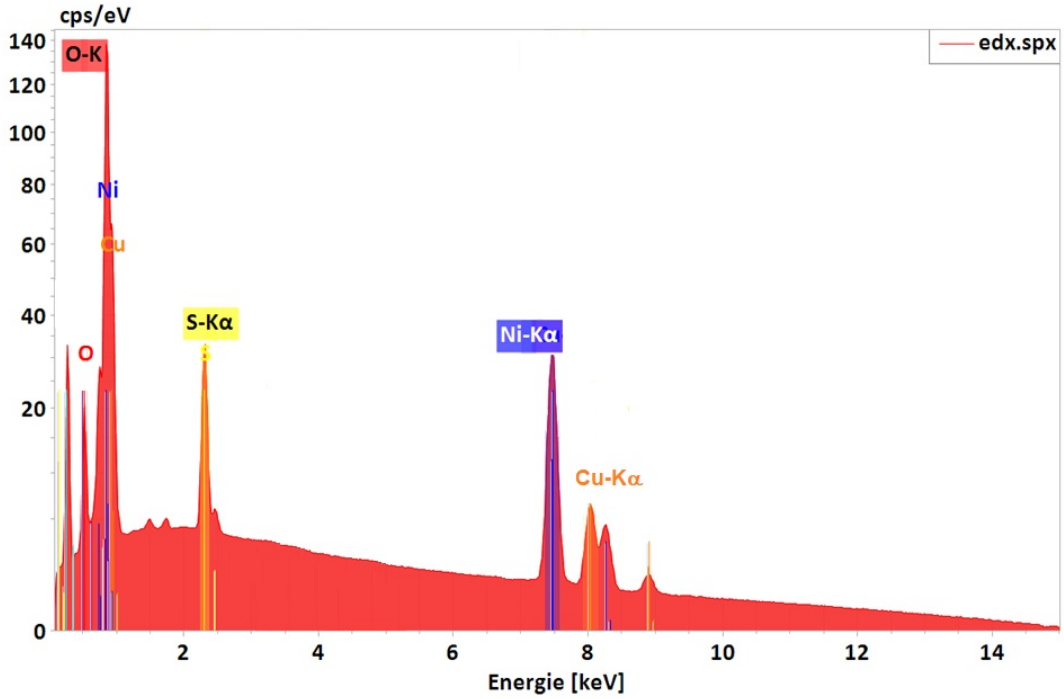

Figure S23. EDX analysis of Cu_9S_5 after OER that depicts the presence of Cu and S. Peak for O presumably appeared due to the formation of CuO on the surface of the Cu_9S_5 as active species for electrolytic OER.

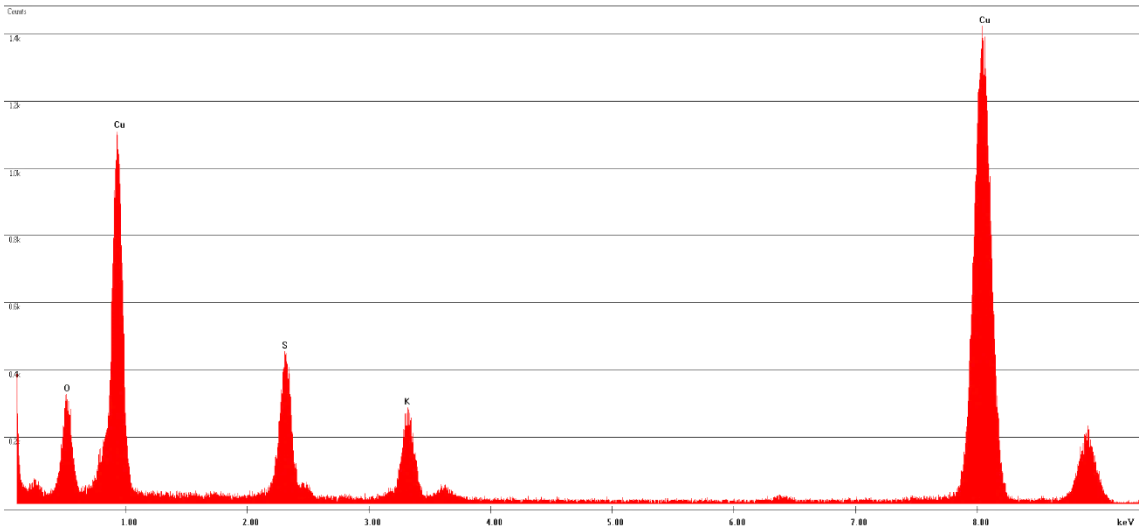

Figure S24. EDX analysis of Cu_9S_5 after OER CA that depicts the presence of Cu and S. Additional peak for O appeared from due to the formation of CuO on the surface of the Cu_9S_5 as active species for electrolytic OER. An additional peak of K appears from the surface adsorbed KOH from the electrolyte solution.

Table S8. The concentration of Cu and S on the KOH electrolyte after 12 h OER CA experiment.

Element	**% element loss in solution**		**Cu:S ratio film (EDX)**
	%Cu	**%S**	
Cu_9S_5 (before CA)	0%	0%	~1.78 0.99
Cu_9S_5 (OER CA)	~7%	~21%	~1.59 : 1

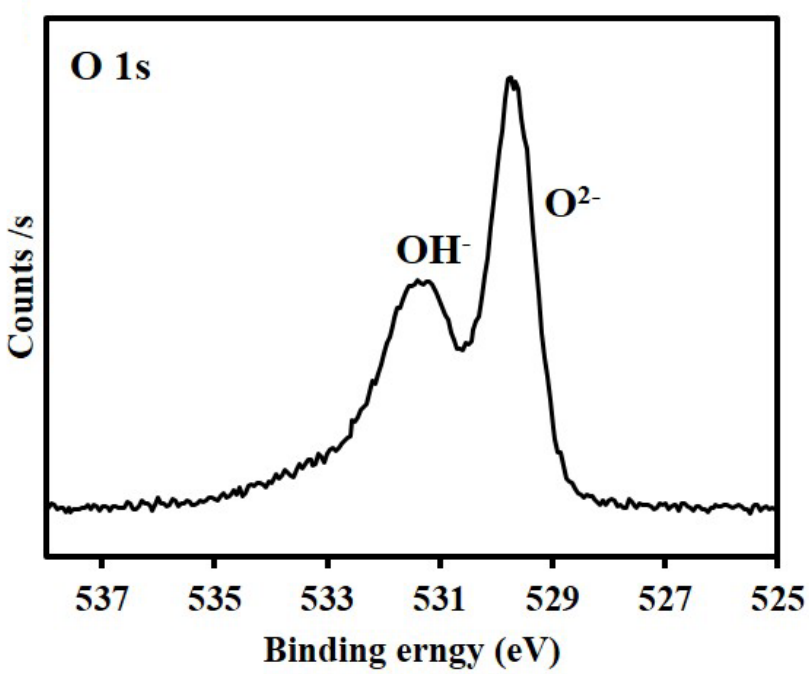

Figure S25. High-resolution core-level XPS spectra of O 1s of Cu_9S_5 after OER CA for 10 h at a constant potential of 1.55 V vs. RHE. Strong O 1s peaks with two prominent energy values for O^{2-} (529.8 eV) and OH^- (531.5 eV) indicate the formation of CuO.[11,29] (OH- presumably appear from the surface adsorbed water molecule and some hydroxide from KOH solution).

References

[1] G. M. Sheldrick, *Program for Crystal Structure Determination;* Universität Göttingen (Germany), **1997**.

[2] L. J. Barbour, *J. Supramol. Chem.* **2001**, *1*, 189–191.

[3] P. Halder, S. Ghorai, S. Banerjee, B. Mondal, A. Rana, *Dalton Trans.* **2017**, *46*, 13739–13744.

[4] L. An, L. Huang, P. Zhou, J. Yin, H. Liu, P. Xi, *Adv. Funct. Mater.* **2015**, *25*, 6814–6822.

[5] a) A. B. F. Martinson, S. C. Riha, E. Thimsen, J. W. Elam, M. J. Pellin, *Energy Environ. Sci.* **2013**, *6*, 1868; b) L. He, D. Zhou, Y. Lin, R. Ge, X. Hou, X. Sun, C. Zheng, *ACS Catal.* **2018**, *8*, 3859–3864;

[6] a) G. Tuci, C. Zafferoni, A. Rossin, L. Luconi, A. Milella, M. Ceppatelli, M. Innocenti, Y. Liu, C. Pham-Huu, G. Giambastiani, *Catal. Sci. Technol.* **2016**, *6*, 6226–6236; b) Y. Zhao, L. Zhao, K. X. Yao, Y. Yang, Q. Zhang, Y. Han, *J. Mater. Chem.* **2012**, *22*, 19726;

[7] a) K. Morimoto, *Am. Mineral.* **1963**, *48*, 110; b) G. Donnay, J. D. H. Donnay, G. Kullerud, *Am. Mineral.* **1958**, *43*, 228–242; c) W. Bryks, E. Lupi, C. Ngo, A. R. Tao, *J. Am. Chem. Soc.* **2016**, *138*, 13717–13725; d) A. Itzhak, E. Teblum, O. Girshevitz, S. Okashy, Y. Turkulets, L. Burlaka, G. Cohen-Taguri, E. Shawat Avraham, M. Noked, I. Shalish, G. D. Nessim, *Chem. Mater.* **2018**, *30*, 2379–2388;

[8] Y. Zuo, Y. Liu, J. Li, R. Du, X. Han, T. Zhang, J. Arbiol, N. J. Divins, J. Llorca, N. Guijarro, K. Sivula, A. Cabot, *Chem. Mater.* **2019**, *31*, 7732–7743.
[9] X. Zhao, L. Liu, Y. Zhang, H. Zhang, Y. Wang, *Nanotechnology* **2017**, *28*, 345402.
[10] X. Liu, S. Cui, M. Qian, Z. Sun, P. Du, *Chem. Commun.* **2016**, *52*, 5546–5549.
[11] X. Liu, S. Cui, Z. Sun, Y. Ren, X. Zhang, P. Du, *J. Phys. Chem. C* **2016**, *120*, 831–840.
[12] M. Qian, X. Liu, S. Cui, H. Jia, P. Du, *Electrochim. Acta* **2018**, *263*, 318–327.
[13] X. Ren, X. Ji, Y. Wei, D. Wu, Y. Zhang, M. Ma, Z. Liu, A. M. Asiri, Q. Wei, X. Sun, *Chem. Commun.* **2018**, *54*, 1425–1428.
[14] S. Wei, K. Qi, Z. Jin, J. Cao, W. Zheng, H. Chen, X. Cui, *ACS omega* **2016**, *1*, 1367–1373.
[15] A. Han, H. Zhang, R. Yuan, H. Ji, P. Du, *ACS Appl Mater. Interfaces* **2017**, *9*, 2240–2248.
[16] B. K. Kim, S.-K. Kim, S. K. Cho, J. J. Kim, *Appl. Catal. B* **2018**, *237*, 409–415.
[17] X. Xiong, C. You, Z. Liu, A. M. Asiri, X. Sun, *ACS Sustainable Chem. Eng.* **2018**, *6*, 2883–2887.
[18] N. Dalai, B. Mohanty, A. Mitra, B. Jena, *ChemistrySelect* **2019**, *4*, 7791–7796.
[19] J. Qi, W. Zhang, R. Xiang, K. Liu, H.-Y. Wang, M. Chen, Y. Han, R. Cao, *Adv. Sci.* **2015**, *2*, 1500199.
[20] K. Fominykh, P. Chernev, I. Zaharieva, J. Sicklinger, G. Stefanic, M. Döblinger, A. Müller, A. Pokharel, S. Böcklein, C. Scheu, T. Bein, D. Fattakhova-Rohlfing, *ACS nano* **2015**, *9*, 5180–5188.
[21] G. Wu, W. Chen, X. Zheng, D. He, Y. Luo, X. Wang, J. Yang, Y. Wu, W. Yan, Z. Zhuang, X. Hong, Y. Li, *Nano Energy* **2017**, *38*, 167–174.
[22] F. Song, M. M. Busch, B. Lassalle-Kaiser, C.-S. Hsu, E. Petkucheva, M. Bensimon, H. M. Chen, C. Corminboeuf, X. Hu, *ACS Cent. Sci.* **2019**, *5*, 558–568.
[23] X. Zhang, B. Zhang, S. Liu, H. Kang, W. Kong, S. Zhang, Y. Shen, B. Yang, *Appl. Surf. Sci.* **2018**, *436*, 974–980.
[24] X. Zhu, T. Jin, C. Tian, C. Lu, X. Liu, M. Zeng, X. Zhuang, S. Yang, L. He, H. Liu, S. Dai, *Adv. Mater.* **2017**, *29*.
[25] K. Fominykh, J. M. Feckl, J. Sicklinger, M. Döblinger, S. Böcklein, J. Ziegler, L. Peter, J. Rathousky, E.-W. Scheidt, T. Bein, D. Fattakhova-Rohlfing, *Adv. Funct. Mater.* **2014**, *24*, 3123–3129.
[26] G.-H. Moon, M. Yu, C. K. Chan, H. Tüysüz, *Angew. Chem. Int. Ed.* **2019**, *58*, 3491–3495.
[27] a) Q. Kang, L. Vernisse, R. C. Remsing, A. C. Thenuwara, S. L. Shumlas, I. G. McKendry, M. L. Klein, E. Borguet, M. J. Zdilla, D. R. Strongin, *J. Am. Chem. Soc.* **2017**, *139*, 1863–1870; b) C. C. L. McCrory, S. Jung, J. C. Peters, T. F. Jaramillo, *J. Am. Chem. Soc.* **2013**, *135*, 16977–16987;
[28] Y. Yoon, B. Yan, Y. Surendranath, *J. Am. Chem. Soc.* **2018**, *140*, 2397–2400.
[29] a) J. Du, F. Li, Y. Wang, Y. Zhu, L. Sun, *ChemElectroChem* **2018**, *5*, 2064–2068; b) T. N. Huan, G. Rousse, S. Zanna, I. T. Lucas, X. Xu, N. Menguy, V. Mougel, M. Fontecave, *Angew. Chem. Int. Ed.* **2017**, *56*, 4792–4796;